

Computational Models of Material Interfaces for the Study of ESWT

Kirsten Fagnan *

Randall J. LeVeque [†]

Thomas J. Matula [‡]

February 24, 2013

Abstract

Extracorporeal Shock Wave Therapy (ESWT) is a noninvasive treatment used to treat a variety of musculoskeletal ailments. A shock wave is generated in water and then focused using an acoustic lens or reflector so the energy of the wave is concentrated in a small treatment region where mechanical stimulation enhancing healing. In this work we have computationally investigated shock wave propagation in ESWT by solving a Lagrangian form of the isentropic Euler equations in the fluid and linear elasticity in the bone using high-resolution finite volume methods. We solve a full three-dimensional system of equations and use adaptive mesh refinement to concentrate grid cells near the propagating shock. We can model complex bone geometries, the reflection and mode conversion at interfaces, and the the propagation of the resulting shear stresses generated within the bone. We discuss the validity of our simplified model and present results validating this approach.

*Lawrence Berkeley National Laboratory, 1 Cyclotron Road, Berkeley, CA 94720

[†]Department of Applied Mathematics, University of Washington, Box 352420, Seattle, WA 98195

[‡]Applied Physics Laboratory, University of Washington, Seattle, WA 98195

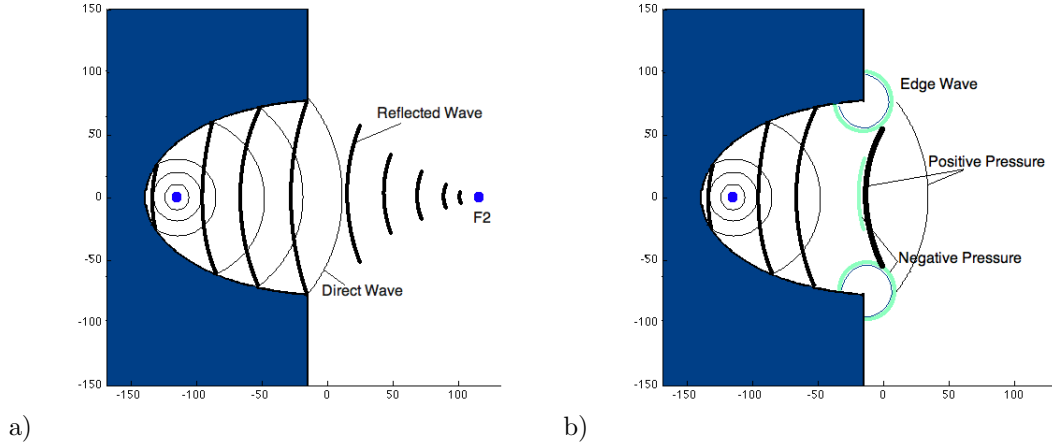


Figure 1: Cartoon of the Dornier HM3 Lithotripter. In a) the spherical wave is generated at F1, reflects off the ellipsoid and the reflected wave focuses at F2. In b) the diagram illustrates the creation of the edge waves at the corner of the ellipsoid and the contribution of negative pressure to the tail of the ESWT pressure wave.

1 Introduction

Extracorporeal shock wave therapy (ESWT) is a noninvasive treatment used to treat musculoskeletal conditions such as bone fractures that fail to heal (non-unions), necrotic wounds, and strained tendons. In this treatment a shock wave is generated in water and then focused using an acoustic lens or reflector so that the energy of the wave is concentrated in a small treatment region. This technique has been used since the 1980's, more widely in Europe and Asia than in the US, where it is still considered experimental and has limited FDA approval. Although the underlying biological mechanisms are not well understood [?], the mechanical stress of cells caused by the propagating shock wave is thought to initiate the release of substances such as VEGF (vascular endothelial growth factor) that cause angiogenesis and neo-vascularization, and hence to increased oxygen supply to damaged tissue, or of similar osteogenic growth factors in bone. The medical shock wave devices are similar to those used for extracorporeal shock wave lithotripsy (ESWL), a widely-used non-surgical treatment for kidney stones in which the focused shock waves have sufficient amplitude to pulverize the kidney stone. In shock wave therapy the amplitudes are generally smaller and the goal is mechanical stimulation rather than destruction, although in some applications such as the treatment of heterotopic ossifications (see ho) larger amplitudes may be used.

Figure ?? shows the geometry of a laboratory shock wave device modeled on the clinical Dornier HM3 lithotripter. The three-dimensional axisymmetric geometry consists of an ellipsoidal reflector made out of metal and a cavity filled with water. A spark plug at the focus of the ellipse marked F1 generates a bubble which collapses and creates a spherical shock wave that reflects and focuses at F2. The major and minor axes of the ellipsoid in the HM3 are $a = 140\text{mm}$ and $b = 79.8\text{mm}$, respectively. The foci of this ellipse are at $(\pm 115, 0, 0)$ and the reflector is truncated at 100mm from F1, or $(-10, 0, 0)$.

In the laboratory, this reflector is immersed in a bath of water and objects can be placed at the second focus of the ellipsoid, F2. This device is in use at the Center for Industrial and Medical Ultrasound (CIMU) at the University of Washington Applied Physics Laboratory and we have used this geometry in order to compare directly with some laboratory experiments.

Computationally, we use this geometry to calculate the initial condition by solving two-dimensional axisymmetric Euler equations with the Tamman equation of state (see eos). These initial conditions are then fed into a full three-dimensional calculation near the focus at F2.

In addition to the HM3, we have also used the geometry of the hand-held Sanywave device used by our collaborator Dr. Michael Chang. Some sample calculations related to the study of HOs are presented in HO.

In each case, the ESWT pressure wave form that is generated has a similar shape. There is a sharp increase in pressure from atmospheric pressure ($\sim 0.1\text{MPa}$) to a peak pressure ranging from $35 - 100\text{MPa}$ over a very short rise time ($\sim 10\text{ns}$), followed by a decrease in pressure to $\sim -10\text{MPa}$ over $\sim 5\mu\text{s}$. The negative fluid pressure in the tail can lead to cavitation bubbles, as discussed below.

Computational models for shock wave propagation and focusing can aid in the study of ESWT. In particular, there are many open questions concerning the interaction of shock waves with complex three-dimensional geometries such as bone embedded in tissue. Because of the difference in material properties, a wave hitting the tissue/bone interface will be partially reflected, and the transmitted wave will have a modified strength and direction of propagation. This can greatly affect the location and size of the focal region as well as the peak pressure amplitude. Moreover, although the shock wave is primarily a pressure wave in soft tissue (which has a very small shear modulus), at a bone interface mode conversion takes place and shear waves as well as compressional waves are transmitted into the bone. These shear waves may be important in biological stimulation. An additional effect is the formation and collapse of cavitation bubbles that can cause tissue damage. While the shock wave is a compression wave, it is followed by a rarefaction wave of expansion, and in the tail the fluid pressure typically drops to negative values. Reflection at interfaces can lead to enhanced regions of expansion and to sufficiently negative pressures that cavitation bubbles can form.

To better understand all of these effects, it is desirable to have a three-dimensional computational model that can simulate the focusing of nonlinear shock waves and their interaction with arbitrarily complex interfaces between different materials.

In this paper we present an approach to this problem that has allowed the study of some of these issues in a simplified context. In particular, we consider an idealized situation in which soft tissue is replaced by water, ignoring its viscoelastic properties, and modeled by the nonlinear compressible Euler equations with the Tamman or Tait equation of state. Bone is modeled as an isotropic and homogeneous linear elastic material.

In reality, soft tissue and bone are very complex multiscale materials with microstructures, inhomogeneities, and anisotropic properties. Any attempt to model the biological effect of shock wave propagation through such materials may require a more sophisticated and detailed model than used here. However, we believe that many of the macro-scale shock propagation issues discussed above can be adequately and most efficiently studied with a simplified model of the form considered here, since the dominant effect we hope to capture is the reflection and transmission of waves at interfaces between materials.

The compressible Euler equations with the Tamman equation of state (see *discussion*) *intwo-dimensionalaxisymmetric*
dimensionalsimulationofthefluid.ThecompressiblefluidequationsarewrittenusingaLagrangianformulationthateasilycou
likematerial.Theresultingequationshavethesameformeverywhere,withadifferentstress-strainrelationshipinthedifere

A high-resolution finite volume method is used to solve these equations. We use the wave-propagation algorithms described in [?] and implemented in Clawpack [?]. These are Godunov-type methods for the hyperbolic system that use solutions to the Riemann problem between adjacent grid cells to determine a set of waves used to update the solution, and second-order correction terms with slope limiters are added to resolve the nearly discontinuous shock waves with minimal smearing or nonphysical oscillation.

These methods are used on a purely rectangular Cartesian grid. Each grid cell has associated with it a set of material parameters determining the material in the cell, in a unified manner so that both fluid and solid can be modeled. Complex geometry is handled by using appropriate averaged values of these parameters in cells that are cut by the interface. This is described further in [?]. Averaging across the interface works quite well when the material properties are sufficiently similar and in [?] we show that this is the case even for fluid/solid boundaries of the type we consider.

We also use patch-based adaptive mesh refinement (AMR) to concentrate grid cells in regions where they are most needed to resolve features of interest. The Clawpack software contains AMR software in both two and three space dimensions and this software has been used directly for the two-dimensional axisymmetric computations of the initial shock wave described in [?]. For the three-dimensional problem we have used ChomboClaw [?], an interface between Clawpack and the Chombo code developed at LBL [?], which provides an implementation of AMR on parallel machines using MPI. Using ChomboClaw, the code originally developed using Clawpack was easily converted into a code that was run on a TeraGrid machine at Texas Advanced Computing Center (TACC) and tested using up to 128 processors.

Extensive laboratory experiments have been performed on shock wave devices to measure the wave form of shock waves produced by various devices, the shape of the focal region, the peak amplitudes of pressure

observed in these regions, and other related quantities. Most of these experiments have been done in a water tank where the shock wave propagates and focuses in a homogeneous medium where measurements are easily done, or with phantoms that are placed in the water as a proxy for bones or kidney stones, with instrumentation such as pressure gauges or photographs used to explore the interaction of the shock wave with the object. In some cases high-speed photographs of the shock wave have been obtained. Creating phantoms from clear bi-refrangent materials and using polarized light it is even possible to photograph the shock wave propagating through the object [?]. We have used some of these experiments to help validate our numerical approach (see ??).

Other researchers have also developed computational models for shock wave therapy and lithotripsy. In prior work the pressure field has been modeled using linear and nonlinear acoustics as well as the Euler equations with the Tait equation of state. Hamilton [?] used linear geometrical acoustics, which holds under the assumption of weak shock strength, to calculate the reflection of the spherical wave. The diffraction of the wave at the corner of the reflector was calculated using the Kirchoff integral method. Christopher's [?] model of the HM3 lithotripter used Hamilton's result as a starting point and considered non planar sources. Coleman et al [?], Averkiou and Cleveland [?] used models based on the KZK equation. Tanguay [?] solved the full Euler equations and incorporated cavitation effects as well as the edge wave.

Our approach differs from these in that we consider the wave propagation in both the fluid and solid by solving a single set of equations that can model both materials. This approach allows us to investigate not only compression and tension effects of ESWT, but also the propagation of shear waves in the solid. Sapozhnikov and Cleveland [?] have investigated the effect of shear waves on spherical and cylindrical stones using linear elasticity with a plane wave initial condition. This initial condition is an unfocused wave, which yields good results for small objects, but would fail to capture the full ESWT pressure wave interaction with three-dimensional bone geometries.

Summary of results in this paper....

2 Model equations

Much of the previous work on ESWT has been centered around the use of the Euler equations with the Tait or Tamman equations of state. These equations of state are typically used for modeling underwater explosions like the spark plug source of the lithotripter device [?, ?]. In this section we discuss the full Euler equations and proceed to show why the Tait equation of state is sufficient for modeling ESWT. Since this equation of state is only a function of the density, ρ , we show how it can be modeled within the framework of linearized elasticity, which enables us to model both the fluid and solid with a single system of equations.

In two space dimensions the Euler equations take the form

$$\frac{\partial}{\partial t}q + \frac{\partial}{\partial x}f(q) + \frac{\partial}{\partial y}g(q) = 0, \quad (1)$$

with

$$q = \begin{bmatrix} \rho \\ \rho u \\ \rho v \\ E \end{bmatrix}, \quad f(q) = \begin{bmatrix} \rho u \\ \rho u^2 + p \\ \rho uv \\ u(E + p) \end{bmatrix}, \quad g(q) = \begin{bmatrix} \rho v \\ \rho uv \\ \rho v^2 + p \\ v(E + p) \end{bmatrix}. \quad (2)$$

Here u and v denote the velocities in the x and y direction, respectively. The total energy is $E = \rho e + \frac{1}{2}(u^2 + v^2)$, and the total enthalpy is $H = h + \frac{1}{2}(u^2 + v^2)$.

Several of the problems we investigated are axially symmetric and this enabled us to reduce the three-dimensional equations to a two-dimensional form. If we first rewrite the equations in cylindrical coordinates (r, θ, z) and then assume no variation and zero velocity in the θ direction, the system we obtain is reduced to two variables, r and z .

$$\frac{\partial}{\partial t} \begin{bmatrix} \rho \\ \rho u_r \\ \rho u_z \\ E \end{bmatrix} + \frac{\partial}{\partial r} \begin{bmatrix} \rho u_r \\ \rho u_r^2 + p \\ \rho u_r u_z \\ u_r(E + p) \end{bmatrix} + \frac{\partial}{\partial z} \begin{bmatrix} \rho u_z \\ \rho u_r u_z \\ \rho u_z^2 + p \\ u_z(E + p) \end{bmatrix} = \begin{bmatrix} -(\rho u_r)/r \\ -(\rho u_r^2)/r \\ -(\rho u_r u_z) \\ u_r(E + p)/r \end{bmatrix}, \quad (3)$$

where u_r and u_z denote the velocities in the r and z directions, respectively. These equations are of the same form as (??), with the addition of geometric source terms that are a result of the variable transformation.

2.1 Equation of State

In order to solve the system (??) or (??), we need to close the system with a relation between the pressure and conserved variables. We have used the Tait [?] and Tammann [?] equations of state, which are applicable to a wide range of liquids. It has been common practice to use the Tait EOS in shock wave therapy and lithotripsy models [?, ?]. This may seem surprising considering the treatment relies upon shock waves to deliver energy and mechanical forces, which typically require a non-isentropic EOS. The Tammann equation of state is valid for non-isentropic flow and experiments have shown that two equations of state agree in the isentropic flow regime [?]. In the event that the shock is weak, or there is only a very small change in the entropy, an equation of state that only depends on the density, such as the Tait equation of state, can be used. Several studies have indicated that in ESWT, there is no significant change in density or pressure as a result of the change of entropy across the shock [?] for pressures ranging from 1 – 200 MPa. This indicates that the use of the Tait equation of state should be sufficient for the study of ESWT.

The Tait equation of state is

$$p = p(\rho) = B \left[\left(\frac{\rho}{\rho_0} \right)^n - 1 \right], \quad (4)$$

where B is a pressure constant that is a weak function of entropy, but is typically treated as a constant, n is a constant playing a similar role to that of γ in the ideal gas law, ρ is the density, and p the pressure.

The Tammann equation of state can be written as

$$p = p(\rho, e) = (\gamma - 1)\rho e - \gamma p_\infty, \quad (5)$$

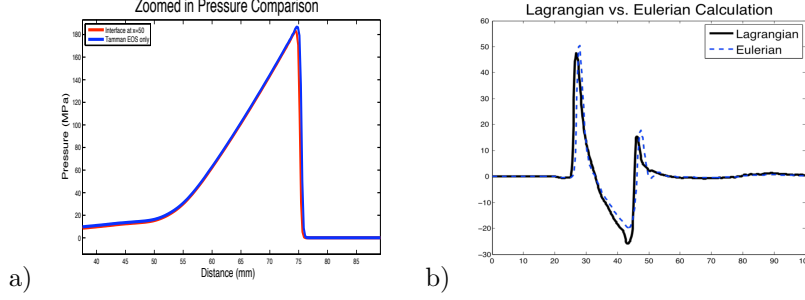


Figure 2: a) Comparison of a pressure wave calculation performed using both the Tait and Tammann equations of state. The results are nearly identical. b) Comparison of the pressure pulse at F2 obtained in the Euler calculation (red dashed curve) and the Lagrangian calculation (blue curve). It is clear that the two sets of equations give good agreement. The wave in the Lagrangian case is slightly attenuated, but this may be due to error in initializing the calculation. In these calculations $\Delta x = 0.5mm$.

where p, ρ and e are the pressure, density and specific internal energy, respectively. The values in water for the pressure constant, p_c , and polytropic constant, γ , are the same as B and n in the Tait equation of state. This equation is similar to the ideal gas law, and reduces to the ideal gas law in the case where $p_\infty = 0$ and $1 < \gamma < 2$.

If it is possible to use the Tait EOS in our model, the equations (??) can be further simplified, reducing the computational complexity of our simulations. Therefore, we performed a numerical investigation of the propagation of a shock wave when modeled by both the Tammann and Tait equation of state. Figure ?? a) shows the result from one experiment where a shock wave with peak over pressure of ≈ 180 MPa has propagated through water. The blue wave represents the result from solving with the Tammann equation of state and the red represents the solution with the Tait equation of state, the pressure profiles are nearly identical. This gives us confidence that the calculations we are interested in can be done by solving the Euler equations with the Tait equation of state, and we can therefore neglect the equation for energy

$$\frac{\partial}{\partial t} \begin{bmatrix} \rho \\ \rho u \\ \rho v \end{bmatrix} + \frac{\partial}{\partial x} \begin{bmatrix} \rho u_r \\ \rho u^2 + p \\ \rho uv \end{bmatrix} + \frac{\partial}{\partial y} \begin{bmatrix} \rho w_z \\ \rho uv \\ \rho v^2 + p \end{bmatrix} = \begin{bmatrix} 0 \\ 0 \\ 0 \end{bmatrix}. \quad (6)$$

and the Lagrangian calculation (blue curve). It is clear that the two sets of equations give good agreement. The wave in the Lagrangian case is slightly attenuated, but this may be due to error in initializing the calculation. In these calculations $\Delta x = 0.5mm$.

2.2 Elasticity equations

In the case of infinitesimal or small displacements, it is possible to write the elasticity equations as

$$\epsilon_t - u_x = 0 \quad (7)$$

$$\rho_0 u_t - \sigma(\epsilon)_x = 0 \quad (8)$$

where the higher order terms in the deformation tensor have been neglected. This form of the equations still allows for nonlinear behavior to be incorporated through the stress-strain relationship, $\sigma(\epsilon)$. We take advantage of this formulation in order to incorporate the nonlinear Tait equation of state in the fluid.

In the case of a fluid where the shear modulus is zero, the stress tensor can be written as $\sigma(\epsilon) = -pI$, where p is the pressure in the fluid and I is the identity matrix. In the case of ESWT, the pressure only depends on changes in the density, and we can rewrite $p(\rho)$ as a function of the strain tensor ϵ . In the case of small deformations, we have that

$$\rho = \frac{\rho_0}{\det(F)} = \frac{\rho_0}{1 + tr(\epsilon)}, \quad (9)$$

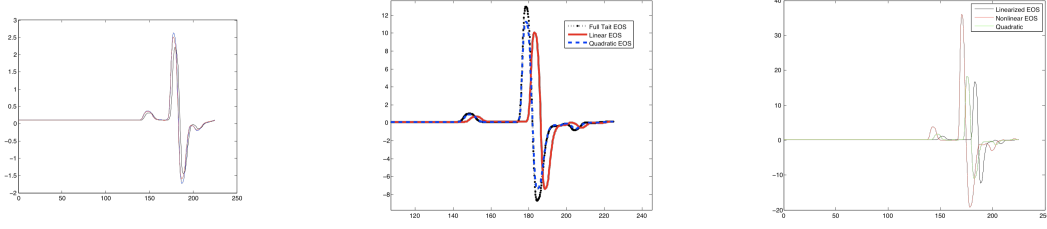


Figure 3: I will make these look better later if we decide to include them. I'm trying to think of a better plot... maybe error vs. amplitude or something like that to just summarize the results

where F is the deformation gradient tensor.

If we plug this into the Tait equation of state (??) we get

$$p(\rho) = p(\epsilon) = B \left[\left(\frac{1}{1 + tr(\epsilon)} \right)^n - 1 \right]. \quad (10)$$

Therefore, in the fluid, we get the following for our stress-strain relationship

$$\sigma(\epsilon) = -(B \left[\left(\frac{1}{1 + tr(\epsilon)} \right)^n - 1 \right]) I \quad (11)$$

This is only valid in the case where the displacements are small, so we calculated the maximum value of the displacements in a two-dimensional axisymmetric calculation with the Euler equations. We found that for the maximum peak pressure of 50MPa, the corresponding maximum velocity was (look up numerical values from the calculation) 10^{-3} m/s. We then calculated the maximum displacement by integrating the velocity over the time step of the calculation and found this to be on the order of 10^{-5} mm. It is therefore reasonable to assume that the density in each grid cell is essentially constant, $\rho = \rho_0$ and that the Lagrangian framework of the elasticity equations will be valid for the fluid. To test this, we took the same initial condition for the 2D axisymmetric Euler equations with the Tamman equation of state and the corresponding 2D axisymmetric Lagrangian form of the equations with the Tait equation of state and measured the pressure at the focus, F2. The results in Figure ?? b) demonstrate reasonably good agreement between the two cases, but the Lagrangian form is slightly attenuated. This may be due to conversion of the initial condition from the conserved variables in the Euler equations (??) to those in the elasticity equations (??).

Since the displacements are so small, it may be reasonable to use a linearized version of the Tait equation of state in our calculations, so then we would be able to simply use the linear elasticity equations. If we assume a small perturbation to the strain, $\epsilon + \delta\epsilon$, we can write the (??) as

$$p(\epsilon) = p_0 + p'(\delta\epsilon)\epsilon + \frac{p''(\delta\epsilon)}{2}\epsilon^2 + \text{H.O.T.} \quad (12)$$

What we call the linear Tait EOS is just the first two terms of (??) and the quadratic Tait EOS is the first three terms. We found that for smaller amplitude waves, the linear Tait EOS is insufficient for predicting the correct arrival time or amplitude. If we include the quadratic term, then we can accurately determine the arrival time, but the amplitude is still incorrect. As we increase the amplitude of the pressure wave, i.e. there is a larger jump in pressure across the shock, neither the linear nor quadratic EOS can capture the correct arrival time or amplitude. This is demonstrated in Figure ??.

For the linear isotropic solid, we use Hooke's law

$$\begin{aligned}\sigma^{11} &= C_{11}\epsilon^{11} + C_{12}\epsilon^{22} + C_{13}\epsilon^{33} \\ \sigma^{22} &= C_{21}\epsilon^{11} + C_{22}\epsilon^{22} + C_{23}\epsilon^{33} \\ \sigma^{33} &= C_{31}\epsilon^{11} + C_{32}\epsilon^{22} + C_{33}\epsilon^{33} \\ \sigma^{12} &= C_{44}\epsilon^{12} \\ \sigma^{13} &= C_{55}\epsilon^{13} \\ \sigma^{23} &= C_{66}\epsilon^{23}.\end{aligned}$$

where the scalar coefficients C_{ij} are determined by the properties of the material being modeled. The parameters used for the bone model were found in [?].

With these two stress-strain relations and the methodology discussed in numerics, we are able to model ESWT with one system of equations.

model, we are confident that the two systems of equations should agree for the weak shocks present in ESWT. We performed an axisymmetric calculation with the Euler equations using the Tammann equation of state to generate an initial condition for the experiment. We then measured the focused wave form at $x = 115.0$ for both the Eulerian and Lagrangian form of the equations. In Figure ?? b) we see that the two models give nearly the same solution, however, the wave from the Lagrangian calculation has been slightly attenuated.

3 Numerical Methodology

We used the wave-propagation algorithms described in [?] and implemented in CLAWPACK [?] to solve the system ???. In this section we provide the basic details of the numerical methodology and approximate solution to the Riemann problem with a spatially-varying flux function, similar to what was done in [?] We also discuss computational issues that necessitate the use of Adaptive Mesh Refinement.

3.1 Approximate Riemann Solver

In order to apply the high-resolution wave propagation algorithms described in [?, ?] to equations (??), we must first determine the solution to the Riemann problem. Recall that the Riemann problem is the initial value problem for a hyperbolic system of conservation laws,

$$q_t + f(q)_x = 0,$$

with special initial data consisting of two constant states separated by a discontinuity

$$q_0(x) = \begin{cases} q_l & \text{if } x < 0 \\ q_r & \text{if } x > 0 \end{cases}.$$

For nonlinear systems of equations, such as (??) this is often most efficiently done through the use of an approximate Riemann solver [?].

The approximate Riemann solver is developed using an approach that has been successfully applied to conservation laws of the form

$$q_t + f(q, x)_x = 0, \tag{13}$$

where $f(q, x)$ is a spatially-varying flux function. The flux function is how we incorporate different equations of state, or stress-strain relations, to model the different materials. The Riemann problem between computational grid cells $i - 1$ and i is based on two flux functions $f_{i-1}(q)$ and $f_i(q)$, as well as the data Q_{i-1} and Q_i . In the case considered below, there are always at least two so-called P-waves in the Riemann solution. One wave \mathcal{W}^1 propagating to the left with speed $s^1 = -c_p < 0$ and \mathcal{W}^2 propagating to the right with speed $s^2 = c_p > 0$. In the solid there may be four additional shear or S-waves propagating at speeds

$\pm c_s$. If the shear modulus is zero, there will be 7 zero-speed stationary waves, otherwise there will only be 3. These waves are taken to be of the form $\mathcal{W}^j = \alpha^j r^j$ for $j = 1 \dots 9$. In our case, the vectors r^j are taken to be the eigenvectors of a linearized problem $f'(q, x)$ and α^j are scalar coefficients. The α^j are typically determined by solving $Q_i - Q_{i-1} = R\alpha$, where R is the matrix of eigenvectors r^j . However, since we have a spatially-varying flux function, we determine these scalars by solving $f_i(Q_i) - f_{i-1}(Q_{i-1}) = R\beta$. Then, using β^j we get $\alpha^j = \beta^j / s^j$. The full details of the so-called *f-wave decomposition* can be found in [?].

In general, the solution to the Riemann problem will have the structure detailed in Figure ???. This particular case shows the solution where two neighboring grid cells have different stress-strain relationships. (explain in greater detail and include diagram)

3.2 Solution of the Riemann Problem for 3D Nonlinear Elasticity

The full three-dimensional system of equations for the Isentropic Euler equations in Lagrangian coordinates is

$$\begin{aligned}
(\epsilon_{11})_t &= \frac{\partial u}{\partial x} \\
(\epsilon_{22})_t &= \frac{\partial v}{\partial y} \\
(\epsilon_{33})_t &= \frac{\partial w}{\partial z} \\
(\epsilon_{12})_t &= \frac{1}{2} \left(\frac{\partial u}{\partial y} + \frac{\partial v}{\partial x} \right) \\
(\epsilon_{23})_t &= \frac{1}{2} \left(\frac{\partial v}{\partial z} + \frac{\partial w}{\partial y} \right) \\
(\epsilon_{13})_t &= \frac{1}{2} \left(\frac{\partial u}{\partial z} + \frac{\partial w}{\partial x} \right) \\
\rho u_t &= \frac{\partial \sigma_{11}}{\partial x} + \frac{\partial \sigma_{12}}{\partial y} + \frac{\partial \sigma_{13}}{\partial z} \\
\rho v_t &= \frac{\partial \sigma_{12}}{\partial x} + \frac{\partial \sigma_{22}}{\partial y} + \frac{\partial \sigma_{23}}{\partial z} \\
\rho w_t &= \frac{\partial \sigma_{13}}{\partial x} + \frac{\partial \sigma_{23}}{\partial y} + \frac{\partial \sigma_{33}}{\partial z}.
\end{aligned} \tag{14}$$

We can write this system in the form

$$q_t - A(x, y, z)q_x + B(x, y, z)q_y + C(x, y, z)q_z = 0, \tag{15}$$

where A, B and C are the Jacobians of the flux functions in the x, y and z directions respectively. For the multi-dimensional methods implemented in CLAWPACK, we need the solution to the Riemann problem along slices in each coordinate direction. Here we provide the details for the solution in the x -direction, but the solution in the y and z directions are similar with appropriate perturbations to the B and C matrices.

The corresponding Jacobian for this system in the x -direction is

$$A(q) = f'(q) = - \begin{pmatrix} 0 & 0 & 0 & 0 & 0 & 0 & \frac{1}{\rho} & 0 & 0 \\ 0 & 0 & 0 & 0 & 0 & 0 & 0 & 0 & 0 \\ 0 & 0 & 0 & 0 & 0 & 0 & 0 & \frac{1}{2\rho} & 0 \\ 0 & 0 & 0 & 0 & 0 & 0 & 0 & 0 & 0 \\ 0 & 0 & 0 & 0 & 0 & 0 & 0 & 0 & \frac{1}{2\rho} \\ \sigma_{\epsilon^{11}}^{11} & \sigma_{\epsilon^{22}}^{11} & \sigma_{\epsilon^{33}}^{11} & 0 & 0 & 0 & 0 & 0 & 0 \\ 0 & 0 & 0 & \sigma_{\epsilon^{12}}^{12} & 0 & 0 & 0 & 0 & 0 \\ 0 & 0 & 0 & 0 & 0 & \sigma_{\epsilon^{13}}^{13} & 0 & 0 & 0 \end{pmatrix} \tag{16}$$

The Jacobians in the y - and z - directions are similar with the entries perturbed appropriately.

We have made use of the fact that the derivative of σ^{11} with respect to the shear strain will be zero in either the Euler or elastic equations. Similarly, the derivative of σ^{12} or σ^{13} will be non-zero only when taken with respect to the shear strains ϵ_{12} and ϵ^{13} , respectively.

The eigenvalues for system (??) are

$$\lambda^{1,2} = \left(\pm \sqrt{\frac{\sigma_{\epsilon^{11}}^{11}}{\rho_0}} \right); \quad \lambda^{3,4} = \pm \sqrt{\frac{\sigma_{\epsilon^{12}}^{12}}{2\rho_0}}; \quad \lambda^{5,6} = \pm \sqrt{\frac{\sigma_{\epsilon^{13}}^{13}}{2\rho_0}}; \quad \lambda^{7,8,9} = 0. \quad (17)$$

The corresponding eigenvectors for system (??) are

$$\begin{pmatrix} 1 \\ 0 \\ 0 \\ 0 \\ 0 \\ 0 \\ \pm\sqrt{\rho_0\sigma_{\epsilon^{11}}^{11}} \\ 0 \\ 0 \end{pmatrix}, \begin{pmatrix} 0 \\ 0 \\ 0 \\ 1 \\ 0 \\ 0 \\ \pm\sqrt{2\rho_0\sigma_{\epsilon^{12}}^{12}} \\ 0 \\ 0 \end{pmatrix}, \begin{pmatrix} 0 \\ 0 \\ 0 \\ 0 \\ 0 \\ 1 \\ \pm\sqrt{2\rho_0\sigma_{\epsilon^{13}}^{13}} \\ 0 \\ 0 \end{pmatrix}, \begin{pmatrix} -\frac{\sigma_{\epsilon^{22}}^{11}}{\sigma_{\epsilon^{11}}^{11}} \\ 1 \\ 0 \\ 0 \\ 0 \\ 0 \\ 0 \\ 0 \\ 0 \end{pmatrix}, \begin{pmatrix} -\frac{\sigma_{\epsilon^{33}}^{11}}{\sigma_{\epsilon^{11}}^{11}} \\ 0 \\ 1 \\ 0 \\ 0 \\ 0 \\ 0 \\ 0 \\ 0 \end{pmatrix}, \begin{pmatrix} 0 \\ 0 \\ 0 \\ 0 \\ 1 \\ 0 \\ 0 \\ 0 \\ 0 \end{pmatrix}. \quad (18)$$

The weights that we need to determine the wave strengths in the wave propagation algorithm found by solving $R\beta = f(Q_r) - f(Q_l)$ are found by solving

$$\begin{pmatrix} 1 & 0 & 0 & 1 & 1 & 0 & 0 & 0 & 1 \\ 0 & 0 & 0 & -\frac{\sigma_{\epsilon^{11}}^{11}}{\sigma_{\epsilon^{22}}^{11}} & 0 & 0 & 0 & 0 & 0 \\ 0 & 0 & 0 & 0 & -\frac{\sigma_{\epsilon^{11}}^{11}}{\sigma_{\epsilon^{33}}^{11}} & 0 & 0 & 0 & 0 \\ 0 & 1 & 0 & 0 & 0 & 0 & 0 & 1 & 0 \\ 0 & 0 & 0 & 0 & 1 & 0 & 0 & 0 & 0 \\ 0 & 0 & 1 & 0 & 0 & 0 & 1 & 0 & 0 \\ -\sqrt{\sigma_{\epsilon^{11}}^{11}\rho_0} & 0 & 0 & 0 & 0 & 0 & 0 & 0 & \sqrt{\sigma_{\epsilon^{11}}^{11}\rho_0} \\ 0 & -\sqrt{2\rho_0\sigma_{\epsilon^{12}}^{12}} & 0 & 0 & 0 & 0 & 0 & \sqrt{2\rho_0\sigma_{\epsilon^{12}}^{12}} & 0 \\ 0 & 0 & -\sqrt{2\rho_0\sigma_{\epsilon^{13}}^{13}} & 0 & 0 & 0 & \sqrt{2\rho_0\sigma_{\epsilon^{13}}^{13}} & 0 & 0 \end{pmatrix} \begin{pmatrix} \beta^1 \\ \beta^2 \\ \beta^3 \\ \beta^4 \\ \beta^5 \\ \beta^6 \\ \beta^7 \\ \beta^8 \\ \beta^9 \end{pmatrix} = \begin{pmatrix} f^1 \\ f^2 \\ f^3 \\ f^4 \\ f^5 \\ f^6 \\ f^7 \\ f^8 \\ f^9 \end{pmatrix}. \quad (19)$$

The solution of the Riemann problem shows that we should expect 9 waves. We will get two P-waves that travel at the speed $\pm c_p$, four S-waves with speeds $\pm c_s$ and 3 stationary waves. In the case of a fluid, there are no S-waves, so we get seven stationary waves. For the wave-propagation algorithms implemented in CLAWPACK, we only use the waves with non-zero speeds for the updates.

3.3 Transverse solvers

The method described here is based on propagating waves normal to each interface. In reality, the waves will propagate in a multidimensional manner and affect cell averages in cells above and below those that are directly adjacent to the interface. In order to include these transverse effects, each fluctuation is split into two transverse fluctuations. This transverse decomposition of the fluctuations can be viewed as solving a second Riemann problem in the transverse direction, even though it is not based on left and right states as we normally think of for a Riemann solver. Once we have determined the transverse fluctuations, they can be used to update the fluxes obtained by solving the original Riemann problem. The transverse correction terms also have the effect of improving the stability limit, allowing for a Courant number of 1, relative to the maximum wave speed in any direction.

(Could you suggest the level of detail that should be provided here?)

3.4 Wave speeds

Since we have rewritten the equations in a Lagrangian frame, we checked to be sure that the new sound speeds, or eigenvalues for our Jacobian, are correct. In the case of the Euler equations with the Tait equation of state, $p(\rho) = p(\epsilon) = B[(\frac{1}{(1+\epsilon^{11}+\epsilon^{22}+\epsilon^{33})^n} - 1)]$, we get the following

$$\begin{aligned}\sigma_{\epsilon^{11}} &= Bn \left(\frac{1}{(1 + \epsilon^{11} + \epsilon^{22} + \epsilon^{33})} \right)^{n+1} \\ &= Bn \frac{1}{(1 + \epsilon^{11} + \epsilon^{22} + \epsilon^{33})} \left(\frac{1}{(1 + \epsilon^{11} + \epsilon^{22} + \epsilon^{33})} \right)^n \\ &= \frac{1}{(1 + \epsilon^{11} + \epsilon^{22} + \epsilon^{33})} n(p + B).\end{aligned}\tag{20}$$

If we then substitute $\rho(t) \approx \rho_0$ into our formula for the eigenvalues (??), we get the following for our wave speeds

$$\pm \sqrt{\frac{n(p + B)}{\rho_0}}.\tag{21}$$

In the standard form of the isentropic Euler equations, we would expect eigenvalues of the form

$$\lambda^{1,2} = u \pm c_p,\tag{22}$$

for the acoustic wave speeds, where u is the velocity of the fluid particles and c_p is the speed of sound in the fluid. As demonstrated in Section ??, the velocities of the fluid particles are small, with a maximum value on the order of 10^{-3} m/s directly behind the shock. As a result, we can neglect the particle velocity in our computation without much of an error and then the wave speeds above agree with those from the isentropic Euler equations. Since fluids do not support shear stress the s-wave speed is zero.

For elasticity if we assume that the density ρ is constant throughout a specific material, but can still vary spatially, and denote it ρ_0 , then the eigenvalues are

$$\lambda^{1,2} = \left[\pm \sqrt{-\frac{\sigma_{\epsilon^{11}}}{\rho_0}} \right],\tag{23}$$

where $\sigma_{\epsilon^{11}} = (\lambda + 2\mu)$. This means that we have

$$\lambda^{1,2} = \pm \sqrt{\frac{\lambda + 2\mu}{\rho_0}},\tag{24}$$

which are the correct sound speed for the p-waves in a linearly elastic medium. For the s-waves we get

$$\lambda^{3,4} = \pm \sqrt{\frac{\sigma_{\epsilon^{12}}}{2\rho_0}} = \sqrt{\frac{\mu}{\rho_0}},\tag{25}$$

which is the correct speed for the s-waves in the $x - y$ direction. The case works out similarly for the $x - z$ direction.

3.5 Axisymmetric form of the equations

We used the two-dimensional axisymmetric form of the equations to generate and initial condition for our three-dimensional calculations, as well as for validation of our model.

The three-dimensional equations in cylindrical coordinates are

$$\begin{aligned}
(\epsilon_{rr})_t &= \frac{\partial u}{\partial r} \\
(\epsilon_{\theta\theta})_t &= \frac{u}{r} + \frac{1}{r} \frac{\partial v}{\partial \theta} \\
(\epsilon_{zz})_t &= \frac{\partial w}{\partial z} \\
(\epsilon_{rz})_t &= \frac{1}{2} \frac{\partial u}{\partial z} + \frac{\partial w}{\partial r} \\
(\epsilon_{r\theta})_t &= \frac{1}{2} \frac{\partial v}{\partial r} + \frac{1}{r} \frac{\partial u}{\partial \theta} - \frac{v}{r} \\
(\epsilon_{\theta z})_t &= \frac{1}{2r} \frac{\partial w}{\partial \theta} + \frac{\partial v}{\partial z} \\
\rho u_t &= \frac{1}{r} \frac{\partial \sigma_{r\theta}}{\partial \theta} + \frac{\partial \sigma_{rr}}{\partial r} + \frac{\sigma_{rr} - \sigma_{\theta\theta}}{r} + \frac{\partial \sigma_{rz}}{\partial z} \\
\rho v_t &= \frac{1}{r} \frac{\partial \sigma_{\theta\theta}}{\partial \theta} + \frac{\partial \sigma_{r\theta}}{\partial r} + \frac{2\sigma_{r\theta}}{r} + \frac{\partial \sigma_{z\theta}}{\partial z} \\
\rho w_t &= \frac{1}{r} \frac{\partial \sigma_{z\theta}}{\partial \theta} + \frac{\partial \sigma_{zz}}{\partial z} + \frac{\partial \sigma_{rz}}{\partial r} + \frac{\sigma_{rz}}{r}.
\end{aligned} \tag{26}$$

If we assume that $v = \epsilon_{\theta z} = \epsilon_{r\theta} = 0$ and there is no variation in the θ direction, then the system (??) simplifies to

$$\begin{aligned}
(\epsilon_{rr})_t &= \frac{\partial u}{\partial r} \\
(\epsilon_{\theta\theta})_t &= \frac{u}{r} \\
(\epsilon_{zz})_t &= \frac{\partial w}{\partial z} \\
(\epsilon_{rz})_t &= \frac{\partial u}{\partial z} + \frac{\partial w}{\partial r} \\
\rho u_t &= \frac{\partial \sigma_{rr}}{\partial r} + \frac{\sigma_{rr} - \sigma_{\theta\theta}}{r} + \frac{\partial \sigma_{rz}}{\partial z} \\
\rho w_t &= \frac{\partial \sigma_{zz}}{\partial z} + \frac{\partial \sigma_{rz}}{\partial r} + \frac{\sigma_{rz}}{r}.
\end{aligned} \tag{27}$$

(28)

It is interesting to note here that the strain in the $\theta\theta$ direction is non-zero and in this case is called the *hoop strain*. A uniform radial displacement is not a rigid body motion, as it would be in the two-dimensional plane strain case, but instead produces a circumferential strain. This is because the original circumference of the cylinder is $2\pi r$, but when there is a strain in the radial direction the circumference grows to $2\pi(r + u_r)$, inducing a strain $2\pi u_r / 2\pi r = u_r / r$.

The Jacobian for system (??) in the z -direction is

$$f'(q) = - \begin{pmatrix} 0 & 0 & 0 & \frac{1}{\rho} & 0 & 0 \\ 0 & 0 & 0 & 0 & 0 & 0 \\ 0 & 0 & 0 & 0 & \frac{1}{2\rho} & 0 \\ \sigma_{\epsilon_{rr}}^{rr} & \sigma_{\epsilon_{zz}}^{rr} & 0 & 0 & 0 & 0 \\ 0 & 0 & \sigma_{\epsilon_{rz}}^{rz} & 0 & 0 & 0 \\ 0 & 0 & 0 & 0 & 0 & 0 \end{pmatrix}, \tag{29}$$

and has an eigen-structure that is equivalent to the two-dimensional elasticity equations, with the addition of a second zero-speed eigenvalue.

In this case, the equations for the source terms are

$$\begin{aligned}
 (\epsilon_{\theta\theta})_t &= \frac{u}{r} \\
 \rho u_t &= \frac{\sigma_{rr} - \sigma_{\theta\theta}}{r} \\
 \rho w_t &= \frac{\sigma_{rz}}{r}.
 \end{aligned} \tag{30}$$

(Describe how this is incorporated into the numerical solution)

3.6 Adaptive Mesh Refinement

The pressure waveform found in ESWT contains a very thin region of high pressure that can not be resolved without a highly refined mesh. In Figure ?? we investigated the effect of grid refinement on the shock wave profile and found that with grid resolution greater than 0.25mm, the wave form at F2 was no longer a shock. In order to efficiently calculate a reasonable ESWT waveform, we utilized ChomboClaw [?], which uses the

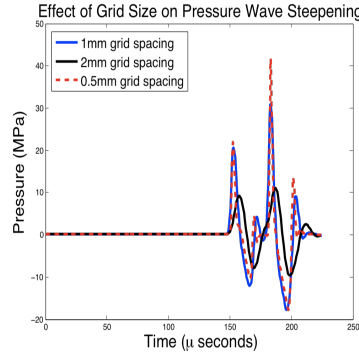


Figure 4: Effect of grid size on shock wave profile

adaptive mesh refinement routines of CHOMBO with the wave propagation solvers of CLAWPACK. This code can be run in parallel using MPI and we ran it on TeraGrid [?] system. It has been indicated that Chombo will scale up to 10,000 processors [?]. We found that the ChomboClaw code scaled up to 128 processors, however we would like to do further testing on a larger system.

3.7 Interfaces and the Cartesian Grid

Calculation series demonstrating the effective use of AMR for capturing the reflection off the curved ellipsoidal geometry of the lithotripter. (Re-running this job to save better plots/pressure waveform, need to save the better resolution run like with the swallow tail focal region calculation.)

4 Results

We have used this approach to model ESWT pressure waves interacting with three-dimensional bone geometries that we assume are comprised of idealized materials. In some cases we model objects identical to those used in laboratory experiments [?], but in others we extracted three-dimensional objects from CT scans of patient data [?]. Here we present results that demonstrate the efficacy of the Lagrangian formulation, as well as examples of calculations performed using real three-dimensional geometries.

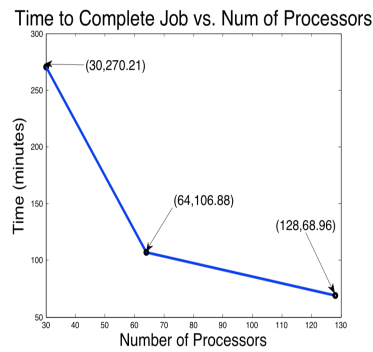


Figure 5: Result from strong scaling test of ChomboClaw up to 128 processors.

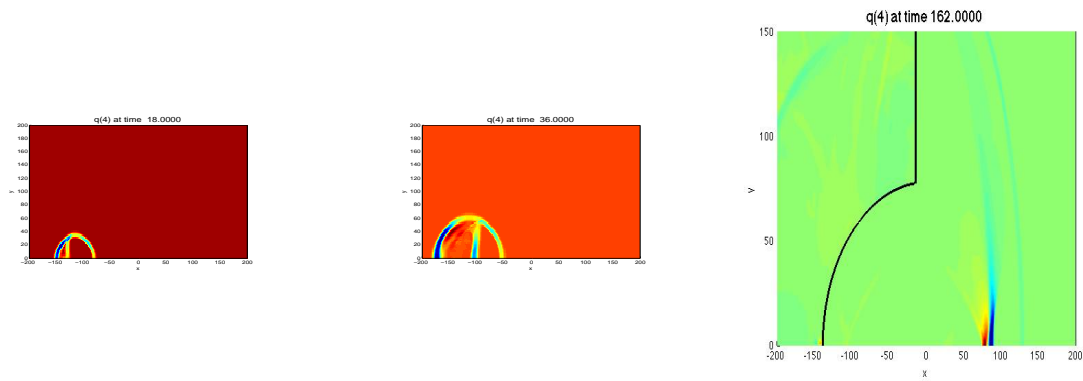


Figure 6: Sample calculations, too coarse, will be replaced with images from a job running now

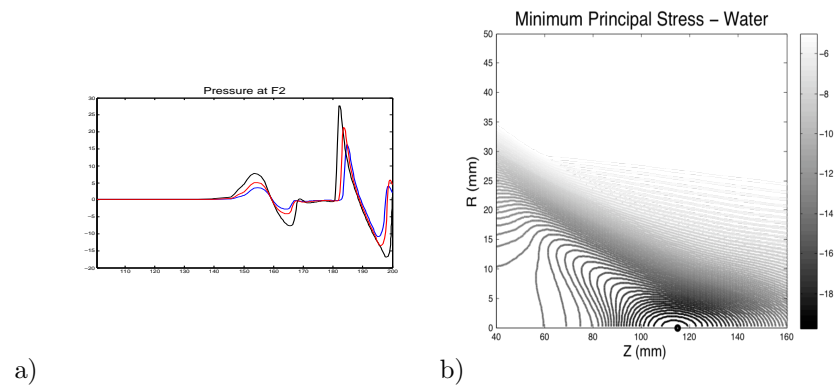


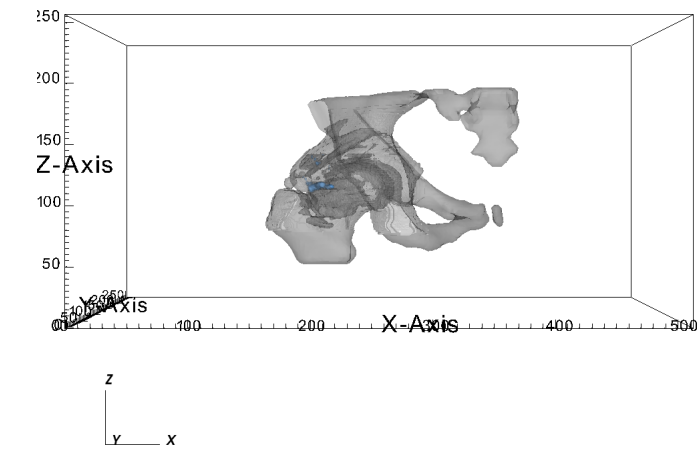
Figure 7: a) Redo with pressure and time-scale labels b) Validation that our Lagrangian code generates the correct cigar shaped region of minimum principal stress, or maximum pressure. This was generated using the 2D Axisymmetric Lagrangian code with the Tait EOS.

4.1 Heterotopic Ossification

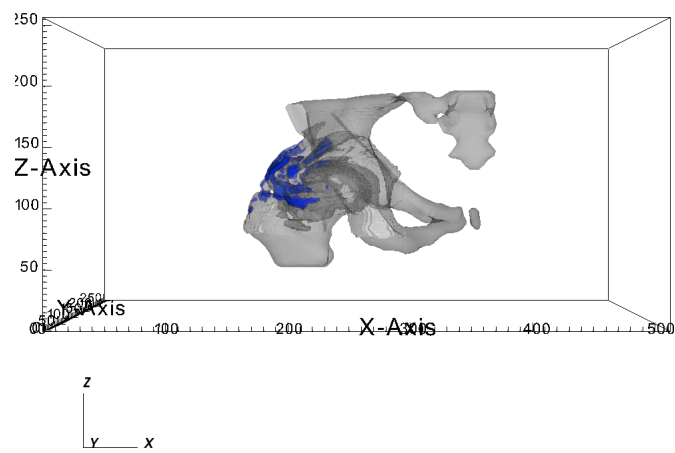
This experiment shows a calculation involving a heterotopic ossification, or a growth of bone-like material in soft tissue that is inhibiting the movement of the hip joint. The composition and material properties of the ossification are not well understood. We are able to use our model to investigate the effect of varying the material properties of the ossification as well as the strength of adhesion to the hip bone. We found that the strength of the adhesion had a significant effect on the location of maximum stress in the object [?]. Here we present a snapshot of the maximum shear and compressive stress calculated in the ossification. (These will be a 3D embedded object, once I have figured out how to plot the stresses on the same figure and have the shading be different - I haven't yet determined how to do that)

Acknowledgements

This work was supported in part by . The authors would like to thank Donna Calhoun and the ANAG group for their assistance with the ChomboClaw calculations.



a)



b)

Figure 8: Isosurface of a) Maximum Compression and b) Maximum Tension in the HO shot directly.